Journal of Power Sources 241 (2013) 783–790

Contents lists available at SciVerse ScienceDirect

Journal of Power Sources

journal homepage: www.elsevier.com/locate/jpowsour

Performance studies of copper–iron/ceria–yttria stabilized zirconia anode for electro-oxidation of butane in solid oxide fuel cells

Gurpreet Kaur, Suddhasatwa Basu*

Department of Chemical Engineering, Indian Institute of Technology Delhi, New Delhi 110016, India

HIGHLIGHTS

- ► Cu–Fe/CeO_2–YSZ anodes with different molar ratios of Cu–Fe fabricated.
- ► Anodes are tested with YSZ electrolyte and LSM/YSZ cathode in H_2 and n-C_4H_{10}.
- ► Performance increases with increase in Fe loading in Cu–Fe/CeO_2–YSZ anodes.
- ► Cell *i*–*V* curves corroborates with the impedance spectroscopy analysis.
- ► Carbon fibre formation found on anode after SOFC operation in butane.

ARTICLE INFO

Article history:
Received 23 November 2012
Received in revised form
21 February 2013
Accepted 25 February 2013
Available online 14 March 2013

Keywords:
Direct hydrocarbon
Solid oxide fuel cell
Butane
Electro-oxidation
Copper–iron/ceria–yttria stabilized zirconia

ABSTRACT

Addition of second metal to Cu is useful for electro-oxidation of hydrocarbons in solid oxide fuel cells (SOFC). In this work, electro-catalysts based on Cu–Fe bimetallic anode for use of both H_2 and n-C_4H_{10} in SOFC is prepared by wet impregnation method into a porous CeO_2–YSZ matrix. The prepared Cu–Fe/CeO_2–YSZ anodes are then characterized by thermo-gravimetric analysis (TGA), X-ray diffraction (XRD), elemental dispersive X-ray (EDX) and scanning electron microscopy (SEM). Carbonaceous deposits formed on Cu–Fe/CeO_2–YSZ anodes after exposure to n-C_4H_{10} are studied using a combination of *i*–*V* characteristics and TGA measurements. It is observed that the addition of Fe to Cu in CeO_2–YSZ cermet anode enhance the performance in H_2 and n-C_4H_{10} fuels. The performance of cell having molar ratio of Cu–Fe of 1:1 in Cu–Fe/CeO_2–YSZ anode shows power density of 240 mW cm^{-2} and 260 mW cm^{-2} in n-C_4H_{10} and in H_2 after n-C_4H_{10} flow at 800 °C. The *i*–*V* curve shows that the conductivity of the anode improves after exposure to n-C_4H_{10}. No apparent degradation in performance is observed after n-C_4H_{10} flow except for carbon fibre formation indicating Cu–Fe bimetallic is worth considering as an anode for direct butane SOFC.

1. Introduction

Solid oxide fuel cell (SOFC) has been emerging as an important class of power generation device as it can be operated on different hydrocarbon fuels through electro-oxidation at anode. Anode supported SOFC has been extensively investigated because of ease of fabrication and high performance. Ni–YSZ cermet anodes of SOFC have showed an excellent catalytic properties and stability for H_2 oxidation but not for hydrocarbons as it results in very fast carbon deposition [1,2]. Carbon deposition covers the active sites of the anode, resulting in rapid irreversible cell deactivation [3]. A significant amount of steam must be needed to induce the steam reforming reactions in order to prevent the carbon deposition but it lowers the electrical efficiency of the system [4]. Alternative anode materials such as Cu/CeO_2–YSZ were thus developed which significantly reduced the coke formation [5–7]. In addition to it, other anode materials like lanthanum strontium titanate [8], lanthanum strontium chromites doped with manganese [9] or ruthenium [10], and $Sr_2Mg_{1-x}Mn_xMoO_{6-\delta}$ [11] showed a stability in hydrocarbons.

The Cu/CeO_2–YSZ anodes have shown a resistance to deactivation from carbon deposition and sulphur poisoning [12,13]. The role of CeO_2 is providing mixed ionic and electronic conductivity in reducing medium because of reduction of Ce^{4+} to Ce^{3+} and showed a beneficial effect when anode is fed with direct hydrocarbons. The carbon deposition reduces because of presence of mobile lattice oxygen in CeO_2 [14,15]. Cu acts as a current collector and is inactive to carbon formation reactions. But the performances of Cu/CeO_2–

* Corresponding author. Tel.: +91 11 26591035; fax: +91 11 26581120.
E-mail address: sbasu@chemical.iitd.ac.in (S. Basu).

0378-7753/$ – see front matter © 2013 Elsevier B.V. All rights reserved.
http://dx.doi.org/10.1016/j.jpowsour.2013.02.083

YSZ anodes in SOFC are lower in H_2 as well as in hydrocarbons. Also, the poor thermal stability because of low melting point of copper affects the anode performance during hours of long run when operating temperature is high. Alloys of Cu with other metals are known to increase the catalytic activity. Cu–Ni alloys showed interesting properties for direct utilization of methane in SOFC [16]. Cu–Co based anodes showed an improved performance in H_2 and n-C_4H_{10} at 800 °C [17]. Recent studies showed improvement in performance as well as stability after addition of Fe in Ni–Fe/GDC based anodes in SOFC using methane [18].

In the present work, Fe as a second metal to Cu is added to check the activity and stability of anode during electrochemical oxidation of n-C_4H_{10}. The anodes based on Cu–Fe/CeO_2–YSZ were prepared by wet impregnation method and tested with H_2 and n-C_4H_{10} fuels with the purpose of analysing the possible use of the anode material for direct hydrocarbon SOFC. The cells used in this study have 10 wt% of CeO_2 and 20 wt% of Cu–Fe having different molar ratios of Cu–Fe [1:0, 3:1, 1:1] in Cu–Fe/CeO_2–YSZ anodes. The cells were tested using YSZ as electrolyte and LSM/YSZ as cathode. The physical characteristics of Cu–Fe/CeO_2–YSZ anode are reported. The carbon deposition was verified by TG analysis. The performance of Cu–Fe/CeO_2–YSZ based SOFC at different temperatures is presented for n-C_4H_{10} fuel and the results of all cells are explained through impedance analysis.

2. Experimental

2.1. Fabrication of SOFC and testing

Cu–Fe/CeO_2–YSZ based anodes, with molar ratios of Cu–Fe of 1:0, 3:1 and 1:1 were prepared by wet impregnation method. The wet impregnation method is adopted to deposit metal in porous YSZ matrix using low sintering temperature as the melting point of Cu is low. The method used to fabricate button type SOFC has been described in detail elsewhere [5] and it is briefly presented here. The dense electrolyte layer of YSZ (Tosoh, 8 mol% Y_2O_3) was casted by tape casting method and then allowed to dry at room temperature for 48 h. The porous YSZ layer was then casted on the top of the electrolyte green tape. The pore formers used to make porous YSZ were graphite (Alfa Aesar, USA) and polystyrene (Acros Organics, USA). Both the layers are then calcined at 1450 °C for 10 h to obtain dense electrolyte layer and porous YSZ matrix. The samples were calcined at a heating rate of 3° min^{-1}. The ratio of pore former to YSZ solid was optimized to get well interconnected bilayers.

The porosity of as prepared porous YSZ was determined to be 70% measured by water uptake method. On the other side of electrolyte, the cathode was painted by slurry containing a 50:50 wt% mixture of YSZ and $La_{0.8}Sr_{0.2}MnO_3$ (LSM), and graphite pore-former followed by calcinations at 1250 °C for 5 h at heating rate of 0.5° min^{-1}. LSM was made in the laboratory by drip pyrolysis method and the procedure of this method has been explained in detail [19]. The calcination at 1250 °C was carried out to avoid any reaction between YSZ and LSM which affects the performance of SOFC [20]. The porous YSZ matrix was impregnated with the aqueous solution of $Ce(NO_3)_3$, $6H_2O$ (Acros Organics, USA) to get 10 wt% of CeO_2 in YSZ. After impregnation, the cells were calcined at 450 °C for 2 h to form the oxides. The calcination at temperature of 450 °C was carried out to prevent increase in crystallite size of ceria when calcined at higher temperature [21]. He et al. [21] showed that ceria flakes present at 450 °C flattened after heating it to 1000 °C. Thus one expect change in morphology of ceria when is operated at a higher temperature. However, He et al. [21] reported that anode (Cu–CeO_2–YSZ) made from ceria calcined at 450 °C gave higher cell performance than that made from cerai calcined at 1000 °C and 1250 °C. Based on this observation calcinations of ceria is fixed to 450 °C. The mixed aqueous solution of $Cu(NO_3)$, $3H_2O$ (Merck, Germany) and $Fe(NO_3)_3$, $9H_2O$ (Alfa Aesar, USA) were then impregnated followed by calcination at 300 °C for 2 h to form the respective oxides of different molar ratios. The impregnation process was repeated until a desired loading of metals was achieved. Following the work of Lv et al. [21(a)], it may be pointed out that there could be some solid reactions between CeO_2 formed at 450 °C and oxides of Cu/Fe formed at 300 °C from the temperature 450 °C to SOFC operating temperature. This issue needs to be investigated further. It is worth mentioning about difficulty in identifying such solid reaction from XRD as very little amount of Cu/Fe oxide species may penetrate into the lattice of CeO_2.

The button cell as prepared has dia of 0.68 cm (area ~0.36 cm^2). The button cell was opened to air on the cathode side, and fuel gas H_2 or n-C_4H_{10} on the anode side. Electronic contacts were formed using silver mesh (Alfa Aesar, USA) and silver paste (Alfa Aesar, USA) at the anode and cathode. The cell was sealed onto alumina tubes using a zirconia-based adhesive (Aremco, 552). The entire cell was then placed inside a furnace and heated to 800 °C at 2 °C min^{-1} in flowing H_2 for reduction of metal oxides to metals in anode. After steady value of open circuit voltage (OCV) was obtained, *i–V* characteristics were recorded in H_2 and n-C_4H_{10} fuels using potentiostat-galvanostat (PGSTAT 30, Autolab) by applying normal linear sweep voltammetry (LSV) at a sweep rate of 5 mV s^{-1}. The *i–V* characteristics were also validated by measuring current and voltage using voltmeter and ammeter under different electronic loads. The H_2 and n-C_4H_{10} were fed to the reactor in dry conditions using flow rate of 40 and 25 ml min^{-1}. Because the area of fuel cells was only 0.36 cm^2, the fuel utilization was less than 1%. Similar fuel utilization has been reported by other investigators [22]. Impedance spectra were collected in potentiostatic mode at OCV using a frequency response analyzer (PGSTAT 30, Autolab) with a frequency range from 100 kHz to 1 Hz with ac signal strength of 10 mV.

2.2. Characterization

The SEM (Zeiss EVO 50, UK) was used to determine morphology and size of the impregnated metal particles in anode. The X-ray diffraction patterns of the prepared anode were recorded by XRD (PW 3040/60, X 'Pert PRO, Netherlands) with an area detector using a Cu Kα radiation source (λ = 1.54056 A°) to study the crystal structure. The 2θ angle ranging from 25° to 70° were explored at a scan rate 3° min^{-1}. The presence of metals in the anode after wet impregnation method was verified by EDX using scanning electron microscope (Zeiss EVO 50, UK). The differential thermal analysis (DTA) and TGA data for an YSZ matrix impregnated with Cu–Fe were obtained using differential thermal analyzer (Netzsch TG 209 F3 Taurus instrument). The deposition of carbon formed during operation of SOFC in n-C_4H_{10} was also verified by TGA. The data was collected from room temperature to 1000 °C at a rate of 10 °C min^{-1}.

3. Results and discussion

3.1. Thermal analysis

TGA for Cu and Cu–Fe impregnated in porous YSZ matrix using their relative precursors is shown in Fig. 1(A–C). In all cases, the complete weight loss took place below 270 °C. It suggests that temperature of approximately 270 °C is required for complete decomposition of nitrates to metal oxides. The DTA curves show the two endothermic peaks for impregnated Cu–Fe having different molar ratio in YSZ. The endothermic peaks are observed at 128 °C and 248 °C for impregnated Cu–Fe in YSZ. First endothermic peak is related to loss of water and second peak is related to formation of

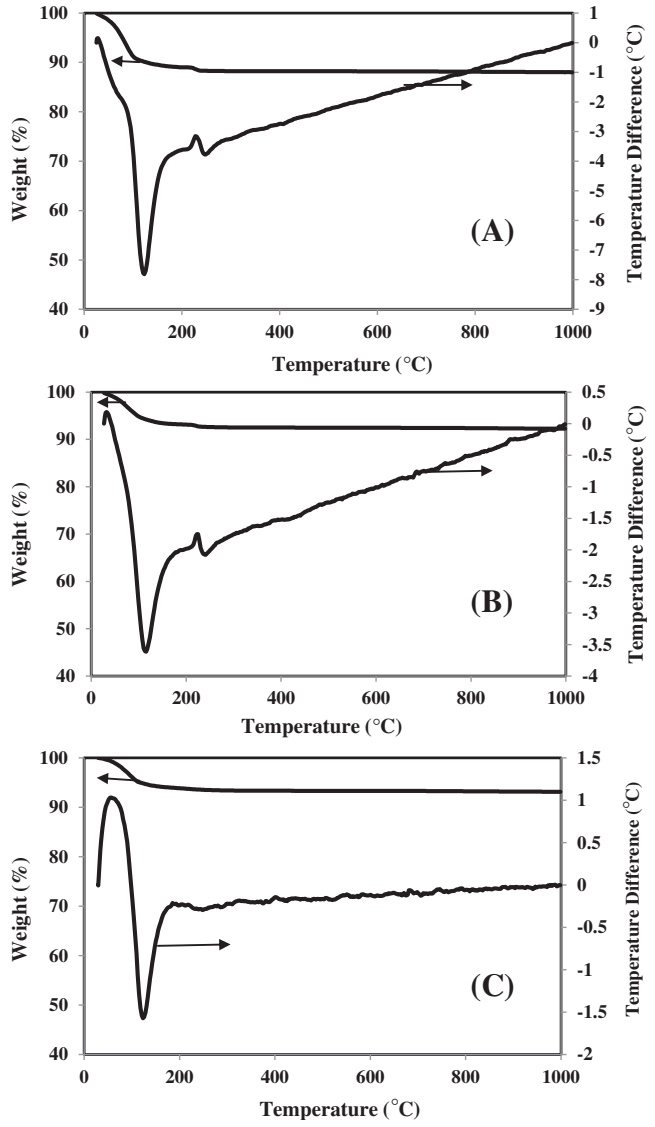

Fig. 1. TGA/DTA of Cu–Fe after impregnation in porous YSZ matrix having molar ratio (A) 1:0 (B) 3:1 (C) 1:1.

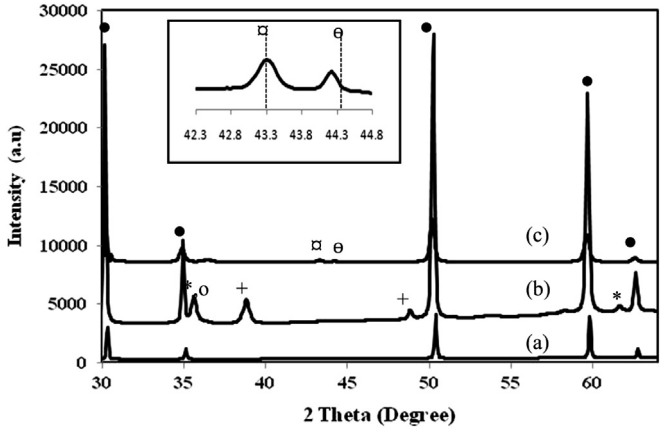

Fig. 2. XRD pattern of (a) YSZ (b) Cu–Fe [1:1] impregnated in YSZ after calcination at 300 °C, (c) Cu–Fe [1:1] impregnated in YSZ after reduction at 800 °C. YSZ (●), Fe_2O_3 (⋆), $CuFe_2O_4$ (○), CuO (+), Cu (¤), Fe (ɵ).

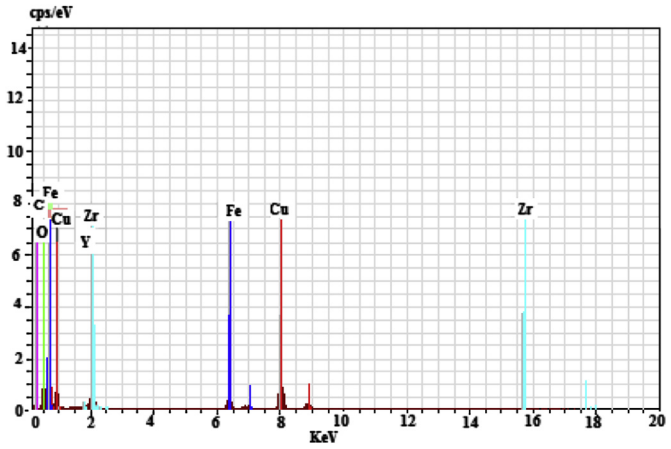

Fig. 3. EDX of Cu–Fe [1:1] impregnated in porous YSZ after reduction in n-C_4H_{10} at 800 °C for 30 min.

Cu–Fe oxides after decomposition of HNO_3 and intermediate products. No peak showing intermediate products is found and it may be due to overlap of peaks at the fast heating rate.

3.2. X-ray diffraction

The XRD patterns of Cu–Fe [1:1] impregnated in YSZ matrix after calcination and reduction in H_2 at different temperatures are shown in Fig. 2. The major peaks at $2\theta = 30.2, 34.9, 50.3, 59.8, 63.1°$ are associated with YSZ. The YSZ peaks are very sharp and confirmed its crystalline nature. The XRD pattern shows the existence of diffraction peaks of Fe_2O_3 and $CuFe_2O_4$ after calcinations at 300 °C. The peaks after reduction in H_2 at 800 °C suggest that at least two phases are formed. The lines drawn at two different positions are expected for the pure Cu and Fe phases. After reduction in H_2, Cu metal segregated from $CuFe_2O_4$ resulting in formation of CuO and Fe_2O_3. Further reduction to Cu and Fe takes place through reduction of CuO and Fe_2O_3 [23]. The peaks at 43.34° and 44.2° are for Cu and Fe. There appears to be small shift in the peaks from their normal positions, implying there is some Fe in Cu phase as expected from phase diagram [24]. Both metals are present in cubic structure. The average particle size of metals extracted from broadening of diffraction peak found from XRD through the well known Debye–Scherrer equation: $d = K\lambda/FWHM \cos\theta$. Where, λ is the wavelength of X-ray (0.154056 nm), θ is the angle at maximum of peak, K is numerical constant with value close to 0.9 and FWHM is the full width at half maximum of the peak expressed in radian. The particle size of Cu and Fe obtained after reduction at 800 °C for 2 h is 0.1–0.15 μm.

3.3. Elemental dispersive X-ray and thermal gravimetric analysis

The EDX analysis of Cu–Fe [1:1] impregnated in porous YSZ after reduction in n-C_4H_{10} for 30 min at 800 °C is shown in Fig. 3. They indicate the presence of Cu, Fe, O, Y, Zr and C. The results indicate the success of fabrication of Cu–Fe–YSZ using wet

Table 1
Effect of composition on carbon formation after reduction in n-C_4H_{10} for 30 min at 800 °C.

Cell no.	Cu–Fe molar ratios and % loading in Cu–Fe/YSZ anodes	Weight gain due to carbon formation (%)
A	Cu:Fe [1:0] – (20 wt%)	<1
B	Cu:Fe [3:1] – (20 wt%)	10
C	Cu:Fe [1:1] – (20 wt%)	16

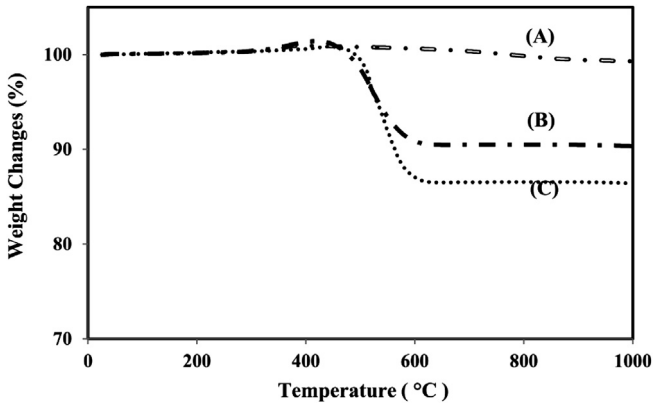

Fig. 4. TGA of Cu–Fe impregnated in porous YSZ after reduction in n-C_4H_{10} at 800 °C for 30 min having molar ratio (A) 1:0 (B) 3:1 (C) 1:1.

impregnation method. Table 1 shows the weight changes on different molar ratio of Cu–Fe in porous YSZ matrix due to carbon formation, after reduction in n-C_4H_{10} flow at 800 °C for 30 min. It should be noted that CeO_2 does not catalyze the formation of carbon in Cu/CeO_2–YSZ anodes [17]. For 20 wt% of Cu–Fe [1:0] in YSZ, negligible weight change was observed but weight gain increases with increase in Fe loading and it is approximately 10 and 16 wt% for Cu–Fe molar ratio of 3:1 and 1:1, respectively. Although it is mentioned earlier that ceria has no role in carbon formation, it actually reduces carbon formation. We observed that carbon formation reduces from 16% to 10% when Cu–Fe/CeO_2–YSZ is used instead of Cu–Fe/YSZ for Cu–Fe ratio 1:1. The reduction carbon deposition is 10%–3% when Cu:Fe ration used is 3:1. The weight gain is because of carbon formation during reduction in n-C_4H_{10} at 800 °C. Fig. 4 shows TGA curve of different molar ratios of Cu–Fe in porous YSZ after reduction in n-C_4H_{10} for 30 min. The curve shows a weight change upto 600 °C, which is attributed to oxidation of metal to metal oxides and deposited carbon to carbon dioxide. The conversion of carbon deposits to CO_2 at low temperature suggests that carbon formed is non graphitic in nature [25].

3.4. Scanning electron microscopy

The microstructure of an anode has a great effect on the performance of the SOFC. Fig. 5(A–C) show the SEM of Cu–Fe/CeO_2–YSZ anode having molar ratio of Cu:Fe of 1:0, 3:1, 1:1 after reduction in H_2 at 800 °C. The SEM images indicate well interconnection between the particles for loading of Cu:Fe of 1:1 in Cu–Fe/CeO_2–YSZ anode, which would be expected to provide better electrical conductivity. Fig. 5(D) shows the SEM of bi-layer porous YSZ and dense electrolyte after calcination at 1450 °C followed by impregnation. It is seen that electrolyte is fully dense. The interface between anode and electrolyte shows good adherence. The thickness of dense layer and porous anode layer is approximately 80 and 170 μm, respectively. The porous anode shows sufficient porosity for diffusion of gases. The anode has large pores with a size of about 40 μm in addition to small pores.

3.5. Electrochemical performance

3.5.1. Performance of cells in n-C_4H_{10} and H_2

The performance of all the three cells having different molar ratios (Table 1) of Cu–Fe in Cu–Fe/CeO_2–YSZ anodes were tested using YSZ electrolyte and LSM/YSZ as cathode in H_2 and n-C_4H_{10} at 800 °C. The anode had initially been exposed to H_2 for 2 h to obtain steady value of OCV and then exposed for 30 min in n-C_4H_{10} before taking *i–V* (current density–voltage) measurements. Both *i–V* and *i–P* (current density-power density) characteristics are shown in Fig. 6. The power density of cell A and B after n-C_4H_{10} flowed for 30 min is 98 and 138 mW cm^{-2} at 800 °C. The power density of cell C is 240 mW cm^{-2}, which is higher than the cell A and B. It has been shown that Cu has no catalytic activity towards oxidation of hydrocarbons [26]. The power density of cell increases with increase in Fe loading in Cu–Fe/CeO_2–YSZ cermet anodes. Also, the cell C shows higher OCV than cell A and B. It has been found that the addition of metals to ceria results in increase in OCV and suggested that nature of intermediates on the reaction surface is affected by catalyst [27]. Fig. 7 shows the X-ray diffraction of Cu–Fe/CeO_2–YSZ

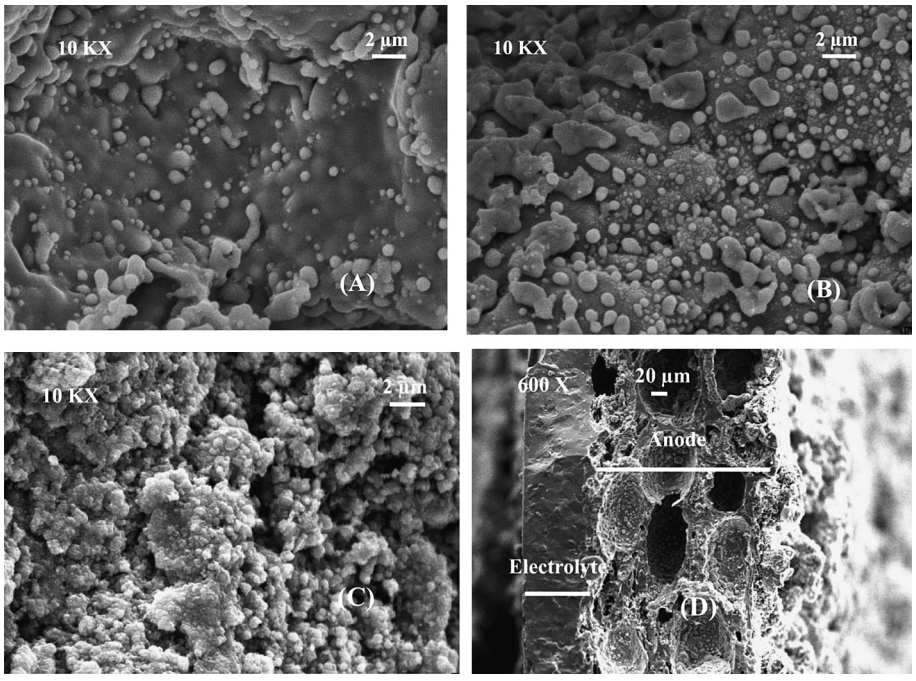

Fig. 5. SEM images of Cu–Fe/CeO_2–YSZ anode with 20 wt% loading in molar ratio of Cu:Fe of (A) 1:0 (B) 3:1 (C) 1:1 (D) bi-layer, dense electrolyte and anode.

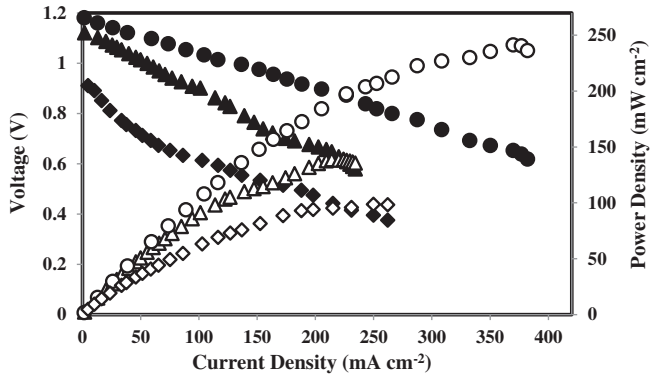

Fig. 6. *I–V* (closed symbols) and *I–P* (open symbols) characteristics in n-C_4H_{10} flow at 800 °C for cell A (◇), cell B (△) and cell C (O). Cell A, B and C have molar ratio of 1:0, 3:1, 1:1 of Cu–Fe in Cu–Fe/CeO_2–YSZ anodes.

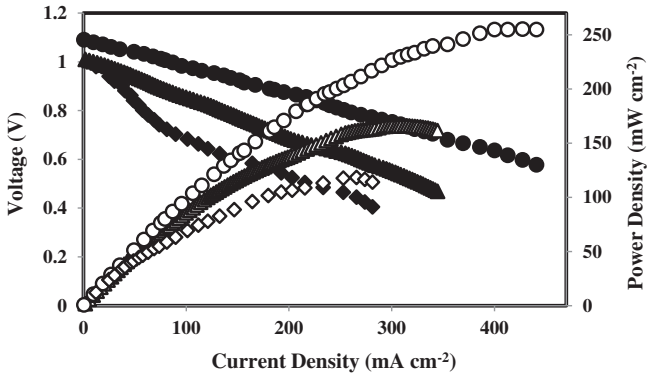

Fig. 8. *I–V* (closed symbols) and *I–P* (open symbols) characteristics in H_2 after n-C_4H_{10} flowed at 800 °C for cell A (◇), cell B (△) and cell C (O). Cell A, B and C have molar ratio of 1:0, 3:1, 1:1 of Cu–Fe in Cu–Fe/CeO_2–YSZ anodes.

cermet anode after reduction at 800 °C. The lattice parameter calculated from XRD peak of CeO_2 is 0.536 nm. The value of lattice parameter is smaller than expected for that of pure CeO_2 (0.541 nm). The difference in lattice parameter suggests that oxygen vacancies are created by substitution of di and tri-valent cations Cu^{2+} and Fe^{3+} in CeO_2 lattice. It has been proven that incorporation of cations in lattice is suitable for hydrocarbon oxidation [28,29]. The increase in OCV and power density with increasing Fe loading in Cu–Fe/CeO_2–YSZ based anodes suggest that intermediate reactions are going towards complete oxidation leading to more effective catalytic ability of cell C for electro-oxidation of n-C_4H_{10}. Because the fuel utilization is less than 1%, it is unlikely that the high OCV can be explained by considering the electrochemical reaction to be occurring through the reforming process and thus suggesting hydrocarbon is oxidized directly. It may also be noted that observed overpotentials is less in cell C than that in cell A and B.

Upon changing the feed to H_2 after n-C_4H_{10} flowed for 30 min, no degradation in the cell performance was observed. The power density is 118, 163, 260 mW cm^{-2} for cell A, B and C as shown in Fig. 8. The performance of cells was somewhat less in n-C_4H_{10} than that in H_2 may be due to high mass of n-C_4H_{10} molecules, which results in slow gas phase diffusion and increased concentration polarization.

The initial performance of cell C in H_2 before n-C_4H_{10} flow was 180 mW cm^{-2} and it increased to 260 mW cm^{-2} in H_2 after n-C_4H_{10} flow as shown in Fig. 9. As the metal loading is low, the enhancement in performance was observed in H_2 after n-C_4H_{10} flow and is mainly due to formation of conductive carbonaceous layer. The conductive carbonaceous species formed during n-C_4H_{10} flow increased the electronic conductivity between metal particles [30]. The nature of carbon film deposited during n-C_4H_{10} flow in cell A, B and C is different from carbon fibres formed on the Ni catalyst [31]. The OCV was observed to be 1.08 V, which is slightly less than the theoretical OCV of ~1.12 V. Since the electrolyte and cathode was same in all the three cells, the performance of the cells depended on the anode characteristics only. Based on the Cu–Fe phase diagram, Cu phase contains some atoms of Fe at 800 °C [23]. These isolated atoms may also provide the catalytic activity for fuel oxidation [28].

3.5.2. Effect of temperature on the performance of cell

Fig. 10 shows the performance of cell C in n-C_4H_{10} at 700 and 800 °C, respectively. The OCV increases with increase in temperature and can be explained by respective Nernst potentials. The power density of cell C increases with the increase in temperature and it is 82 and 240 mW cm^{-2} in n-C_4H_{10} at 700 and 800 °C, respectively. The performance of the cell at different temperature is not only dependent on the anode side reaction but also on the electrolyte and cathode kinetics.

3.6. Electrochemical impedance analysis

Fig. 11(a, b) shows the impedance spectra (complex plane plots) of cell A, B and C in n-C_4H_{10} and H_2 at 800 °C. The high frequency

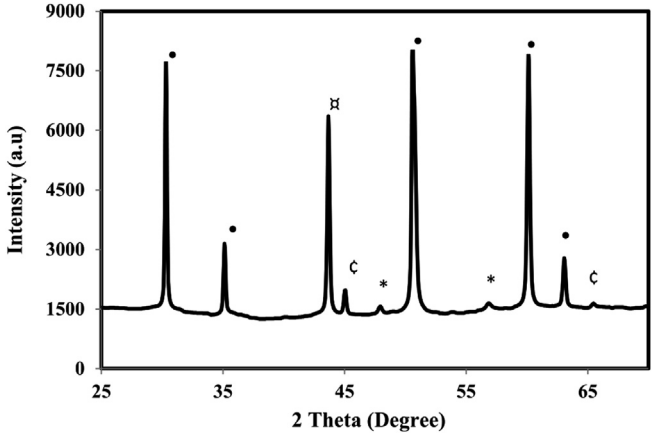

Fig. 7. XRD pattern of Cu–Fe/CeO_2–YSZ anodes having molar ratio of Cu–Fe 1:1 after reduction in H_2 at 800 °C. YSZ (●), Cu (¤), Fe (¢) and CeO_2 (*).

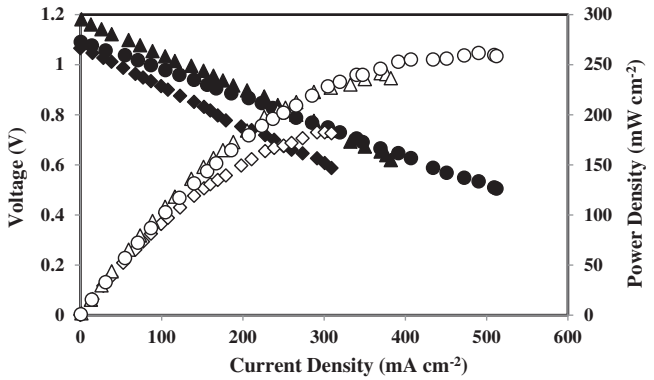

Fig. 9. *I–V* (closed symbols) and *I–P* (open symbols) characteristics of cell C in H_2 before n-C_4H_{10} flow (◇), in n-C_4H_{10} (△) and in H_2 after n-C_4H_{10} flow (O) at 800 °C. Cell C have molar ratio of 1:1 of Cu–Fe in Cu–Fe/CeO_2–YSZ anodes.

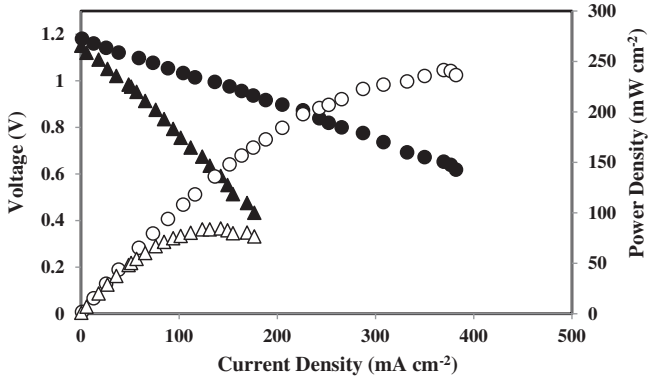

Fig. 10. *I–V* (closed symbols) and *I–P* (open symbols) characteristics for cell C in n-C_4H_{10} at different temperatures: (△) 700 °C, (○) 800 °C. Cell C have molar ratio of 1:1 of Cu–Fe in Cu–Fe/CeO_2–YSZ anodes.

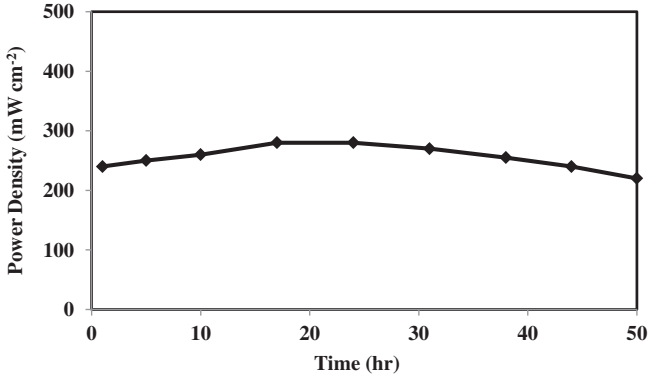

Fig. 12. Power density at 0.6 V as a function of time for cell C operating on n-C_4H_{10} flow at 800 °C.

intercept of the impedance spectra corresponds to the ohmic resistance of electrolyte, anode and cathode, contact resistances between interfaces and between current collector and electrodes. During these measurements, the cathode and electrolyte used were same for both the cells; thus the changes in the impedance spectra are related to changes in the anode side reaction at 800 °C. The large changes in the impedance spectra are observed in low frequency region in cell A, B and C are associated with anode processes. The total resistance at low frequency region is higher for cell A and B than cell C. The resistance at frequency of 2 kHz in an arc is same in cell A, B and C and is due to the cathode processes [32]. The ohmic resistance of all the cells in n-C_4H_{10} was 0.55 Ω cm^2. These values are larger than expected for an 80 μm, YSZ electrolyte at 800 °C. This suggests that the electrodes and current contacts contribute an additional 0.165 Ω cm^2 to the ohmic resistance of the cell.

3.7. Long term performance

In Fig. 12, the power density at 0.6 V is plotted as a function of time for cell C operating on n-C_4H_{10} at 800 °C. During test run of 50 h, a slight increase and then decrease in performance was observed. To investigate the reason behind above changes in performance, the impedance spectra of a different cell C with time is taken and may be noticed in Fig. 13(a, b). During initial hours, both

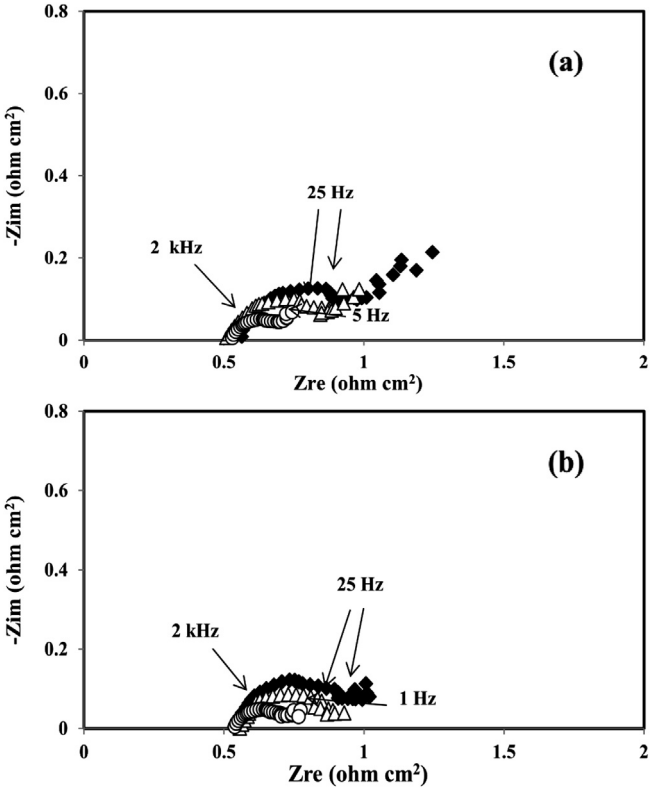

Fig. 11. Impedance spectra for cell A (◆), cell B (△) and cell C (○) In (a) n-C_4H_{10} and (b) H_2 after n-C_4H_{10} at 800 °C. Cell A, B and C have molar ratio of 1:0, 3:1 and 1:1 of Cu–Fe in Cu–Fe/CeO_2–YSZ anodes.

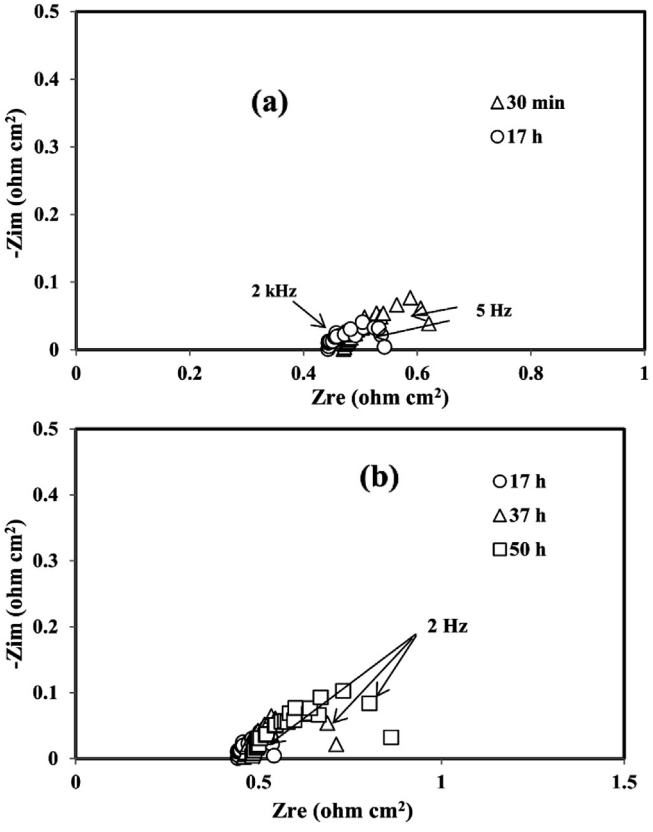

Fig. 13. Impedance spectra of cell having molar ratio of Cu–Fe [1:1] in Cu–Fe/CeO_2/YSZ anodes as a function of time during reduction in n-C_4H_{10} at 800 °C.

ohmic as well as total resistance decreased with time. The decrease in ohmic resistance may be due to better connection between particles by conductive carbonaceous layers. Similar trend has been also observed in Ref. [30]. It may also be pointed out that total resistance of cell C first decreases and then increases with time. SEM and EDX showed carbon fibre formation on the anode surface after operating cell C in n-C_4H_{10} for 50 h as shown in Fig. 14(a, b). It reveals that the carbon formed is sufficient to improve the conductivity but not enough to completely affect the anode structure at the operating conditions. Question is how it is possible? It has been observed by the investigators, who are working on catalytic cracking of hydrocarbon (methane) on Cu–Ni, Cu, Fe, Ni supported on alumina and Ceria, that carbon fibre, filament and MWCNT forms on catalyst surface [33–35]. It is reported that these fibres are hollow in nature and reactant gas can reach to the surface of the catalyst through the interstices of the fibres and through the fibres. It was shown that reactant gases are adsorbed on carbon fibre and it reaches to catalyst surface easily because of their presence [34,35]. A reaction mechanism for such kind of observation is given in Ref. [35]. Carbon fibre formation is also observed by Ye et al. [36] in Cu–CeO2–ScSZ anodes for direct ethanol solid oxide fuel cell but they have not analysed further the role of carbon fibres in ethanol oxidation. The attrition of such carbon fibre from catalyst surface is possible as pointed out by Jang and Cha [37]. It is quite possible similar phenomena is taking place in Cu–Fe/CeO_2–YSZ anode catalyst in the case of direct butane SOFC.

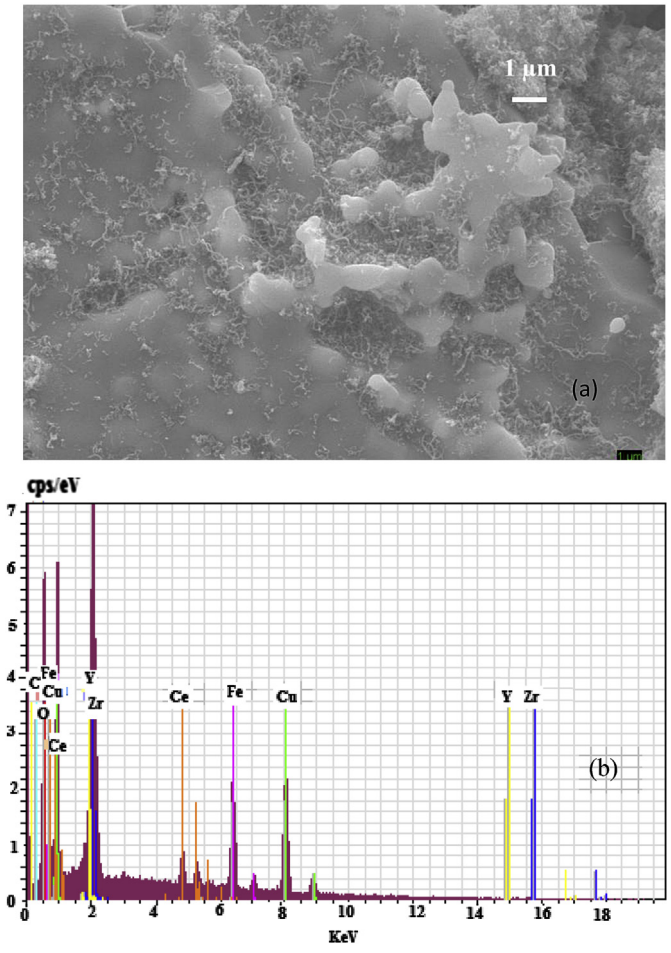

Fig. 14. SEM (a) and EDX (b) Cu–Fe/CeO_2/YSZ anode (Cu–Fe [1:1]) showing carbon fibre formation after operating SOFC in n-C_4H_{10} at 0.6 V and 800 °C during 50 h.

4. Conclusions

The performance of Cu–Fe/CeO_2–YSZ cermet anode having different molar ratios of Cu–Fe [1:0, 3:1, 1:1] in CeO_2–YSZ anodes using YSZ electrolyte and LSM/YSZ as cathode were tested with H_2 and n-C_4H_{10}, respectively. The SEM images show the well interconnection between particles for Cu:Fe [1:1] in porous anode and formation of dense electrolyte. The increase in cell performance in n-C_4H_{10} was observed with the increase in loading of Fe in Cu–Fe/CeO_2–YSZ cermet anodes. The single button cell having molar ratio of Cu:Fe of 1:1 achieved 240 mW cm^{-2} in n-C_4H_{10} at 800 °C. The increase in performance in H_2 after n-C_4H_{10} flow is mainly attributed to increase in conductivity by carbonaceous species formed during n-C_4H_{10} flow. The TGA shows non graphitic nature of carbon formed in Cu–Fe/CeO_2–YSZ anodes and SEM shows formation of carbon fibre formation after 30 min operation in butane. A slight increase and then decrease in performance of cell C with time (50 h) is corroborated with impedance spectra at different times. The performance degradation of cell C in n-C_4H_{10} at 800 °C during 50 h operation is not appreciable and needs further investigation.

Acknowledgements

Authors would like to acknowledge financial support of Council of Scientific and Industrial Research and Ministry of New and Renewable Energy, Govt. of India during execution of the project.

References

[1] H.P. He, J.M. Hill, Appl. Catal. A 317 (2007) 284–292.
[2] Y. Matsuzaki, I. Yasuda, Solid State Ionics 132 (2000) 261–269.
[3] R.T.K. Baker, Carbon 27 (1989) 315–323.
[4] K. Sasaki, Y. Teraoka, J. Electrochem. Soc. 150 (2003) A878–A884.
[5] S. Park, J.M. Vohs, R.J. Gorte, Nature 404 (2000) 265–267.
[6] R.J. Gorte, S. Park, J.M. Vohs, C.H. Wang, Adv. Mater. 12 (2000) 1465–1469.
[7] S. McIntosh, R.J. Gorte, Chem. Rev. 104 (2004) 4845–4865.
[8] O.A. Marina, N.L. Canfield, J.W. Stevenson, Solid State Ionics 149 (2002) 21–28.
[9] J. Liu, B.D. Madsen, Z.Q. Ji, S.A. Barnett, Electrochem. Solid-state Lett. 5 (2002) A122–A124.
[10] B.D. Madsen, W. Kobsiriphat, Y. Wang, L.D. Marks, S.A. Barnett, J. Power Sources 166 (2007) 64–67.
[11] Y.H. Huang, R.I. Dass, Z.C. Denyszyn, J.B. Goodenough, J. Electrochem. Soc. 153 (2006) A1266–A1272.
[12] H.P. He, R.J. Gorte, J.M. Vohs, Electrochem. Solid-State. Lett. 8 (2005) A279–A280.
[13] H. Kim, S. Park, J.M. Vohs, R.J. Gorte, J. Electrochem. Soc. 148 (2001) A693–A695.
[14] I.S. Metcalfe, P.H. Middleton, P. Petrolekas, B.C.H. Steele, Solid State Ionics 57 (1992) 259–264.
[15] V.D. Belyaev, T.I. Politova, O.A. Marina, V.A. Sobyanin, Appl. Catal. A. Gen. 133 (1995) 47–57.
[16] H. Kim, C. Lu, W.L. Worrell, J.M. Vohs, R.J. Gorte, J. Electrochem. Soc. 149 (2002) A247–A250.
[17] S.I. Lee, J.M. Vohs, R.J. Gorte, J. Electrochem. Soc. 151 (2004) A1319–A1323.
[18] H. Kan, H. Lee, Catal. Commun. 12 (2010) 36–39.
[19] P. Gordes, N. Christiansen, E.J. Jensen, J. Villadsen, J. Mater. Sci. 30 (1995) 1053–1058.
[20] A. Mitterdorfer, L.G. Gauckler, Solid State Ionics 111 (1998) 185–218.
[21] H. He, J.M. Vohs, R.J. Gorte, J. Electrochem. Soc. 150 (2003) A1470–A1475; (a) H. Lv, H. Tu, B. Zhao, Y. Wu, K. Hu, Solid State Ionics 177 (2007) 3467–3472.
[22] S.I. Lee, K. Ahn, J.M. Vohs, R.J. Gorte, Electrochem. Solid-state Lett. 8 (2005) A48–A51.
[23] H.C. Shin, S.C. Choi, K.D. Jung, S.H. Han, Chem. Mater. 13 (2001) 1238–1242.
[24] M.A. Turchanin, P.G. Agraval, I.V. Nikolaenko, J. Phase Equilib. 24 (2003) 307–319.
[25] S. McIntosh, J.M. Vohs, R.J. Gorte, J. Electrochem Soc. 150 (2003) A470–A476.
[26] S. McIntosh, J.M. Vohs, R.J. Gorte, Electrochim. Acta 47 (2002) 3815–3821.
[27] S. McIntosh, J.M. Vohs, R.J. Gorte, Electrochem. Solid-State Lett. 6 (2003) A240–A243.
[28] Z. Xing, W. Hua, W. Honggang, L. Kongzhai, C. Xianming, J. Rare Earth 28 (2010) 907–913.
[29] C.S. Chin, W.H. Cheng, S.S. Lin, Appl. Catal. A 257 (2004) 97–106.
[30] S. McIntosh, H. He, S.I. Lee, O.C. Nunes, V.V. Krishnan, J.M. Vohs, R.J. Gorte, J. Electrochem. Soc. 151 (2004) A604–A608.

[31] M.L. Toebes, J.H. Bitter, A.J. van Dillen, K.P. de Jong, Catal. Today 76 (2002) 33–42.
[32] S. McIntosh, J.M. Vohs, R.J. Gorte, J. Electrochem. Soc. 150 (2003) A1305–A1312.
[33] H.F. Abbas, W.M.A. Wan Daud, Int. J. Hydrogen Energy 35 (2010) 1160–1190.
[34] J. Chena, Y. Li, Z. Li, X. Zhang, Appl. Catal. A: Gen. 269 (2004) 179–186.
[35] K. Asai, Y. Nagayasu, K. Takane, S. Iwamoo, E. Yagasaki, K. Ishi, M. Inoue, J. Jpn. Petrol. Inst. 51 (1) (2008) 42–49.
[36] X. Ye, J. Zhou, S.R. Wang, F.R. Zeng, T.L. Wen, Z.L. Zhan, Int J. Hydrogen Energy 37 (2012) 505–510.
[37] H.O. Jang, W.S. Cha, Korean J. Chem. Eng. 24 (7) (2007) 374–377.